Quantifying aerosol direct radiative effect with Multiangle Imaging Spectroradiometer observations: Top-of-atmosphere albedo change by aerosols based on land surface types

Yang Chen,[1,2] Qinbin Li,[1,3] Ralph A. Kahn,[1,4] James T. Randerson,[2] and David J. Diner[1]

Received 9 July 2008; revised 20 October 2008; accepted 10 November 2008; published 24 January 2009.

[1] Using internally consistent albedo, aerosol, cloud, and surface data from the Multiangle Imaging Spectroradiometer (MISR) instrument onboard the Terra satellite, top-of-atmosphere (TOA) spectral albedo change ($d\alpha$) in the presence of aerosols over land is estimated and its dependence on aerosol and surface properties is analyzed. Linear regressions between spectral TOA albedo and aerosol optical depth (AOD) for different surface types are examined to derive the aerosol-free TOA albedo. MISR surface BiHemispherical Reflectance (BHR) values are used to differentiate surface types. We find relatively high correlations between spectral TOA albedo and AOD for BHR-stratified data in $2^\circ \times 2^\circ$ grid cells. The global mean values of cloud-free $d\alpha$ over land for June–September 2007 are estimated to be 0.018 ± 0.003 (blue), 0.010 ± 0.003 (green), 0.007 ± 0.003 (red), and 0.008 ± 0.006 (near-infrared). Individual regions show large variations from these values. Global patterns of $d\alpha$ are determined mainly by AOD and aerosol radiative efficiency. Large positive values of $d\alpha$ are observed over regions with high aerosol loading and large single-scattering albedo, where the aerosol scattering effect is dominant. The presence of light-absorbing aerosols reduces aerosol radiative efficiency and $d\alpha$. Surface reflectance influences both aerosol scattering and absorbing effects. Generally, the aerosol radiative efficiency decreases with increasing BHR. We also examined $d\alpha$-AOD correlations over different vegetation types. We find the smallest $d\alpha$ values are over needleleaf forests and shrublands, whereas the largest values are over cropland and barren regions. The aerosol radiative efficiencies are lowest over needleleaf forests and barren regions and highest over grasslands and croplands.

Citation: Chen, Y., Q. Li, R. A. Kahn, J. T. Randerson, and D. J. Diner (2009), Quantifying aerosol direct radiative effect with Multiangle Imaging Spectroradiometer observations: Top-of-atmosphere albedo change by aerosols based on land surface types, *J. Geophys. Res.*, *114*, D02109, doi:10.1029/2008JD010754.

1. Introduction

[2] Aerosols, both natural and anthropogenic, perturb the radiative balance of Earth's atmosphere directly by scattering and absorbing the solar irradiance [*Chylek and Coakley*, 1974; *Coakley et al.*, 1983; *Charlson et al.*, 1990]. On a global average, anthropogenic aerosols exert a negative radiative forcing, including a total aerosol direct radiative forcing of -0.5 ± 0.4 W m^{-2} [*Intergovernmental Panel on Climate Change*, 2007]. It partly offsets the positive radiative forcing caused by the post-industrial rise of carbon dioxide (1.66 ± 0.17 W m^{-2} [*Intergovernmental Panel on Climate Change*, 2007]), though the spatial distributions of aerosol forcing is very different. An accurate quantification of the aerosol direct radiative forcing is critical for the interpretation of previous climate records and the projection of future climate change [*Mishchenko et al.*, 2007; *Chylek et al.*, 2007].

[3] Current estimates of the aerosol direct radiative forcing have large uncertainties [*Intergovernmental Panel on Climate Change*, 2007]. Aerosol particles have a variety of shapes, sizes, and chemical compositions, that directly affect the aerosol optical properties and the ability of aerosols to change the climate [*Kaufman et al.*, 2002a]. Spatial and temporal distributions of aerosols are highly variable owing to their diverse sources and short lifetimes [*Quinn et al.*, 2000; *Quinn and Bates*, 2005]. Additionally, the land surface is highly heterogeneous in reflecting and absorbing solar radiation at different wavelengths [*Betts et al.*, 1996], which also impacts the aerosol effect on Earth's radiative balance. Thus, estimating aerosol radiative forcing is more challenging than estimating the radiative forcing owing to well-mixed greenhouse gases.

[1]Jet Propulsion Laboratory, California Institute of Technology, Pasadena, California, USA.
[2]Department of Earth System Science, University of California, Irvine, California, USA.
[3]Department of Atmospheric and Oceanic Sciences, University of California, Los Angeles, California, USA.
[4]NASA Goddard Space Flight Center, Greenbelt, Maryland, USA.

Copyright 2009 by the American Geophysical Union.
0148-0227/09/2008JD010754

[4] A large portion of the uncertainty in quantifying aerosol direct radiative forcing results from poor constraints on the aerosol shortwave direct radiative effect (SWDRE). In this paper, we use the term aerosol radiative effect to represent the change in top-of-atmosphere (TOA) radiative fluxes due to the presence of all aerosols (natural and anthropogenic), and distinguish this from aerosol radiative forcing (the radiative effect of anthropogenic aerosols alone). The estimation of SWDRE by all aerosol species is the basis for quantifying the direct radiative forcing by anthropogenic aerosols. Therefore, a first step toward reducing the uncertainty range of aerosol forcing is to improve the estimate of aerosol SWDRE.

[5] Previously, a widely used approach for estimating the aerosol SWDRE is through chemical transport and general circulation model simulations [e.g., *Hansen et al.*, 1998]. There are large uncertainties in these model-based estimates as well as discrepancies among them, due to incomplete knowledge of aerosol processes and assumptions made in the aerosol simulations [*Yu et al.*, 2006; *Kinne et al.*, 2006]. Recently, much effort has also been made to assess the aerosol radiative effect using measurements from ground-based networks, satellite sensors, and intensive aircraft field experiments [*Yu et al.*, 2006]. In particular, satellite remote sensing provides frequent, global coverage of aerosol amount and type, as well as the TOA radiance distribution. It thus offers a unique opportunity to constrain aerosol SWDRE [*Kaufman et al.*, 2002a; *Anderson et al.*, 2005; *Diner et al.*, 2005].

[6] Two approaches have been used to exploit satellite data in the calculation of aerosol SWDRE. In the first approach, satellite aerosol observations are used to feed a radiative transfer model to derive the aerosol radiative effect [e.g., *Yu et al.*, 2004; *Remer and Kaufman*, 2006]. The second approach uses satellite observations directly without resorting to radiative transfer calculations. In this case, the aerosol direct radiative effect is derived from satellite-observed changes in broadband radiative flux due to the presence of aerosols in the atmosphere [*Christopher et al.*, 2000; *Loeb and Kato*, 2002; *Christopher and Zhang*, 2002; *Loeb and Manalo-Smith*, 2005]. However, the satellite-only approach has so far been limited primarily to over the oceans. Application of this approach over land remains challenging mainly because of the large uncertainty in aerosol retrievals over bright land surfaces, the large heterogeneity in land surface reflectivity, and the difficulty to estimate the TOA radiative flux for aerosol-free scenes [*Loeb and Kato*, 2002]. The Multiangle Imaging SpectroRadiometer (MISR) aboard NASA's Terra satellite provides more accurate aerosol optical depth (AOD) retrievals over land [*Abdou et al.*, 2005], as well as more information about aerosol properties [*Kahn et al.*, 2001], than are obtained from single-angle, multispectral techniques. It thus has the potential to reduce aerosol SWDRE uncertainties over land. Recently, *Patadia et al.* [2008] estimated aerosol SWDRE over global land using merged Clouds and Earth's Radiant Energy System (CERES), Moderate Resolution Imaging Spectroradiometer (MODIS), and MISR data. They obtained aerosol-free TOA broadband flux through the regression between MISR single-band AOD and CERES broadband flux for $0.5° \times 0.5°$ cloud-free regions.

[7] In this study, we estimate the aerosol SWDRE on a global scale. Our approach is similar but different in several important ways from that of *Patadia et al.* [2008]. First, we use MISR data for aerosol properties, TOA albedo, surface optical properties, and cloud properties. The use of internally consistent data should reduce systematic sampling biases that can occur when data from different instruments are used. Second, we estimate the aerosol-free TOA albedo separately for different land cover types within a region, thereby taking into account land surface heterogeneity. Finally, we examine the relationship between the spectral TOA albedo and spectral AOD, which may better represent nonlinear wavelength-dependent effects.

[8] This paper is the first in a two-part series. Here we examine the TOA albedo change due to the presence of aerosols over land by analyzing four months of MISR data for June–September 2007. During this period, intense wildfires were observed in central Africa, North America, South America, and Siberia (MODIS hotspot/active fire detections, 2002 data set, from MODIS Rapid Response Project, NASA/GSFC, distributed by University of Maryland, Fire Information for Resource Management System, available at http://maps.geog.umd.edu). Large amounts of light-absorbing aerosols, including black carbon, were emitted from the wildfires. We focus on investigating how the aerosol amount, aerosol optical properties and land surface type affect the spectral aerosol radiative effect. In the companion paper (hereinafter part 2) we will present a method for estimating aerosol broadband SWDRE over the globe. Multiple-year MISR data will be explored and seasonal and interannual variability of aerosol SWDRE will be examined.

[9] Detailed descriptions of MISR data and the methodology used are presented in section 2. The global distribution of TOA albedo change due to aerosols, as well as its dependence on aerosol properties and surface type, is shown in section 3. We present an uncertainty analysis for these calculations in section 4. Summary and conclusions are given in section 5.

2. Data and Methodology

2.1. MISR Data

[10] The MISR sensor uses nine cameras pointed at fixed viewing angles (0°, ±26.1°, ±45.6°, ±60.0°, ±70.5°) to observe reflected and scattered sunlight in four spectral bands: 446 (blue), 558 (green), 672 (red), and 866 nm (near-infrared, NIR) [*Diner et al.*, 1998]. The swath width is ~400 km, which provides global coverage in about 9 days at the equator and 2 days near the poles.

[11] MISR global retrievals of aerosols, TOA albedo, surface properties and cloud information are available since late February 2000. For the purpose of quantifying TOA albedo change by aerosols, four MISR level 2 products are used in this study (Table 1): the aerosol product (AS_Aerosol), the albedo product (TC_Albedo), the land surface product (AS_Land), and the classifier product (TC_Classifier).

[12] We use the "best estimate optical depth" from the MISR Level 2 Aerosol Product (Version 20), which has a spatial resolution of 17.6×17.6 km^2 [*Diner et al.*, 2001] and is reported at four spectral bands as mentioned above. The uncertainties of MISR AOD have been assessed with

Table 1. Summary of MISR Products and Parameters Used in This Study

Product	Parameter	Version	Spatial Resolution (km × km)	Explanation
TC_Albedo	AlbedoLocal[a]	F05_0011	2.2 × 2.2	TOA local albedo, derived from top-leaving bidirectional reflectance factors (BRFs) only
	BRFSide_Mean		2.2 × 2.2	Mean value of BRFs registered to the side of a column
	NumUnobscureSide		2.2 × 2.2	Number of unobscured pixels with BRFs registered to the side of a column
	CloudyClearDesignation		2.2 × 2.2	Cloudy-clear designation determined from Stereoscopically Derived Cloud Mask (SDCM) and Angular Signature Cloud Mask (ASCM)
TC_Classifier	SVMCloudConfidenceLevel	F05_0010	1.1 × 1.1	Support Vector Machine (SVM) derived cloud confidence level
AS_Land	LandBHR	F06_0021	1.1 × 1.1	Bihemispheric reflectance over land
AS_Aerosol	RegBestEstimateSpectralOptDepth	F11_0021	17.6 × 17.6	Best estimated aerosol optical depth
	RegBestEstimateSpectralSSA		17.6 × 17.6	Best estimated aerosol single scattering albedo
	RegBestEstimateAngstromExponent		17.6 × 17.6	Best estimated aerosol angstrom exponent

[a]AlbedoLocal, BRFSide_Mean, NumUnobscureSide, LandBHR, RegBestEstimateSpectralOptDepth, and RegBestEstimateSpectralSSA are available for four spectral bands.

independent measurements. For example, *Liu et al.* [2004] estimated that the MISR AOD retrieval error over land is approximately 0.04 + 0.18 AOD. Thus, for AOD values between 0.1 and 0.5 over land, the expected error in MISR AOD should be within 0.06–0.13. In comparison, the error in the MODIS AOD retrieval over land had been estimated to be 0.05 + 0.2 AOD [*Chu et al.*, 2002]. *Kahn et al.* [2005] showed that about two thirds of the MISR-retrieved AOD values fall within ±20% of concurrent AERONET values. In particular, the MISR retrievals over desert and coastal regions, where surface brightness and subpixel water contamination makes accurate retrievals challenging, are in good agreement with AERONET [*Abdou et al.*, 2005; *Martonchik et al.*, 2004]. Recently, *Liu and Mishchenko* [2008] compared coincident AOD measurements from MISR and MODIS. They showed the agreement over the land is often poor and even unacceptable. However, they acknowledged that their analysis cannot be used to determine which retrieval is more accurate.

[13] MISR also constrains aerosol Single Scattering Albedo (SSA) and Angstrom Exponent (AE). SSA represents the relative importance of aerosol scattering and absorption, and AE contains information about aerosol size. MISR aerosol retrieval method and its sensitivity to SSA have been previously reported [*Chen et al.*, 2008, and references therein]. Uncertainties for AE and SSA are difficult to estimate owing to the lack of validation data. We are currently evaluating these quantities by comparison to AERONET values. The challenge is that there are far fewer AERONET particle property retrievals than AOD retrievals. Additionally, AERONET-derived SSA is not a direct measurement and is subjected to many of the same uncertainties as the satellite retrievals. In this study, we use MISR-derived SSA and AE to study how these aerosol optical properties influence the aerosol ability to modify TOA albedo.

[14] On the basis of observed radiances, MISR generates several TOA albedo products [*Diner et al.*, 1999]. For the present study, we use the TOA local albedo, because it has the highest spatial resolution (2.2 × 2.2 km^2) among all albedo products. MISR assigns recorded upward radiances to the tops and sides of vertical columns, 2.2 × 2.2 km^2 in horizontal extent, at a height given by the Reflecting Level Reference Altitude (RLRA) obtained from stereo-derived cloud top heights. The spectral TOA local albedos from the MISR Level 2 standard product are determined only from the top-leaving radiances. Because the side-leaving, upward radiances are not included, using these albedos would probably cause an underestimation of the aerosol radiative effect. In this study, we include the side contribution by adding back the unobscured side-leaving, upward radiances stored in the MISR TOA Albedo product. The radiances from different cameras are weighted using preestablished solid angle weighting factors [*Diner et al.*, 1999]. To be compatible with the AOD product, we resampled the TOA local albedo (with side contribution included) to the 17.6 × 17.6 km^2 resolution AOD grid. This method is similar to the standard process of deriving MISR restrictive albedo [*Diner et al.*, 1999]. The only difference is that we calculate the albedo for 17.6 × 17.6 km^2 domains, whereas the MISR restrictive albedo was derived on 35.2 × 35.2 km^2 domains. The TOA albedo and AOD for each cloud-free 17.6 × 17.6 km^2 grid box are defined as a "data pair," which will be subject to linear regression analysis as discussed in section 2.2.

[15] In this study we use two different MISR products for cloud screening. In the base case calculation, we use the SVM Cloud Confidence Level (CCL), which was derived using Support Vector Machine (SVM), a machine learning technique [*Mazzoni et al.*, 2007]. The MISR SVM CCL product has a spatial resolution of 1.1 × 1.1 km^2. The 17.6 × 17.6 km^2 grid box is set to "cloudy" if a single value of SVM CCL within the grid box is "highly likely" or "likely." This aggregation of confidence levels is conservative, to minimize the cloud contamination. All plots and tables shown in this paper are derived using SVM CCL cloud masks. As a sensitivity test, we also use the Cloudy Clear Designation (CCD), which was used for determining the azimuthal model in the MISR TOA local albedo standard retrieval. Similarly, we assume a 17.6 × 17.6 km^2 grid box to be cloudy if a single pixel within it is marked with a "cloudy" CCD. The cloudy grid boxes are excluded from further calculations.

[16] The MISR Surface product provides a number of parameters related to land surface properties, which can be used for stratifying by surface type. We use in this study the BiHemispherical Reflectance (BHR), defined as the radiant exitance divided by irradiance ("albedo") under ambient illumination conditions (including both direct and diffuse illumination). This parameter is available in MISR's four

spectral bands. Since MISR retrieval is able to separate the surface from the atmospheric signals, the retrieved BHR will reflect the change in surface optical properties, independent of the aerosols in the atmosphere above. The performance of MISR land surface parameters in classifying vegetation and other surface types has been widely evaluated [e.g., *Hu et al.*, 2007; *Armston et al.*, 2007]. The MISR BHR data has a spatial resolution of 1.1×1.1 km^2, and was also resampled to the 17.6×17.6 km^2 grid for analysis.

2.2. Method

[17] Aerosol effect on the TOA albedo ($d\alpha$) in each $2° \times 2°$ latitude-longitude region is defined as the difference between the mean MISR TOA albedo (α) within the region over the time interval of interest (1 month) and the TOA albedo without the presence of aerosols (α_0). Within each $2° \times 2°$ region, there is little variation in the downward solar flux. Thus we simply estimated α from the arithmetic mean TOA albedo for all data pairs within each $2° \times 2°$ domain. Satellite instruments (including MISR) are not able to observe the aerosol-free TOA albedo directly, since aerosol particles are always present in the atmosphere. To estimate α_0, we perform linear regressions between the spectral TOA albedo and spectral AOD for all the data pairs that have similar aerosol and surface properties. The y intercept of each regression line represents the estimated aerosol-free TOA albedo for that region. We also assess the confidence with which this extrapolation can be performed.

[18] In this study, the regression is performed for data pairs in each $2° \times 2°$ region for each month. This selection of spatial and temporal scales preserves enough data samples and AOD dynamic range for the correlation analysis, and simultaneously limits the large variability in aerosol and surface properties, thus maintaining the quality of the linear regressions for most regions. In addition, considering the large variability of surface reflectance over land, we further divide the data pairs in each $2° \times 2°$ region into different sets according to their BHR values. On the basis of the probability density function of BHR globally (discussed with Figure 3, cell C, in section 3.1), we divide the observed range into 10 evenly distributed sets between 0 and 0.1, and 35 sets between 0.1 and 0.8. We then examine the TOA albedo–AOD regression for data sets stratified by BHR within each region. Since the probability distributions of AOD and BHR are spectrally dependent (see Figure 3, cells B and C, in section 3.1), the linear regression analyses are performed for each spectral band individually.

[19] Figure 1 shows an example of a successful linear regression. The gray points represent all cloud-filtered data pairs associated with AOD and TOA albedo. Since no side contribution is included in the plotted TOA albedo, the correlation is noisy. The inclusion of both the top and side radiance contributions (black points in Figure 1) significantly improves the correlation and reduces the uncertainty in estimating the aerosol-free TOA albedo. The side contribution is particularly important when a thick aerosol layer (e.g., a smoke or dust plume) is clearly present. The regression line in Figure 1 demonstrates that in the blue band, the presence of these aerosols raises the TOA albedo in this region (for a certain BHR stratum) at a rate of 0.074 per unit of AOD, and the derived aerosol-free TOA albedo is 0.161.

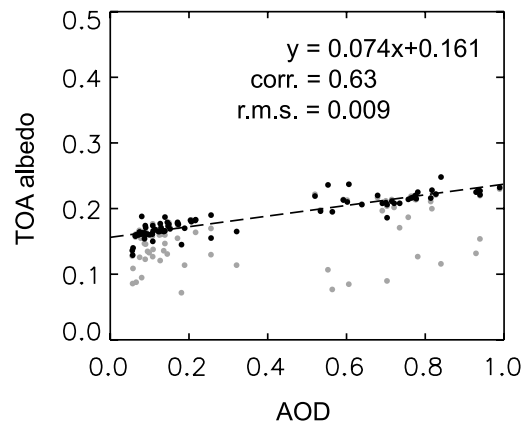

Figure 1. An example of linear regression used for estimating aerosol-free TOA albedo (~60°N, 94°W; 0.04 < BHR < 0.05). Each black dot represents a data pair with spectral (blue band in this case) AOD and TOA albedo (with side contribution). The y intercept of the regression line (dashed line) represents the derived spectral TOA albedo in the absence of aerosols. Grey dots show the data pairs with AOD and TOA albedo from MISR standard product when the side contributions of radiance associated with each RLRA column are not included.

[20] We consider a linear regression successful if the root-mean-square (RMS) error of the regression is smaller than 0.025, or if the correlation coefficient is larger than 0.5. We also require the number of data pairs in each set be greater than 10, and the AOD dynamic range to be over 0.15. Overall, about 70% of the data pairs in the visible bands produce successful regressions. Several reasons can cause a failure in linear regression. Data points may be too few owing to extensive cloud cover or unsuccessful retrievals. Data points may have similar AOD values so that the AOD dynamic range is too small to do the regression. When surface or aerosol properties have large variabilities within a region during a month, a good linear regression between α and AOD is also difficult. The success ratio drops to about 30% for the MISR NIR band. This is likely due to two factors. AODs are typically lower in the NIR than in the visible bands [*Ricchiazzi et al.*, 2006] as a result of smaller aerosol scattering in the former. Additionally, surface reflectivity is higher over some surfaces in the NIR than in the visible bands [*Miura et al.*, 2008].

[21] If the linear regression fails, $d\alpha$ cannot be estimated from the difference between α and α_0, because there is no successful estimate of α_0 for that BHR set within that $2° \times 2°$ region. In such cases, $d\alpha$ is obtained by multiplying the mean AOD for that data set by a scaling factor. The scaling factors were predetermined from all the available successful regressions globally. For each successful regression, we saved the slope of the AOD-α regression and the mean surface BHR and aerosol SSA of the data used for regression. The regressions were classified into different groups on the basis of the mean BHR and SSA values, and the mean value of regression slopes for each group was calculated. We fit an empirical expression for the slope (the scaling factor) in terms of BHR and SSA. This empirical scaling factor, which represents the mean ability of aerosols

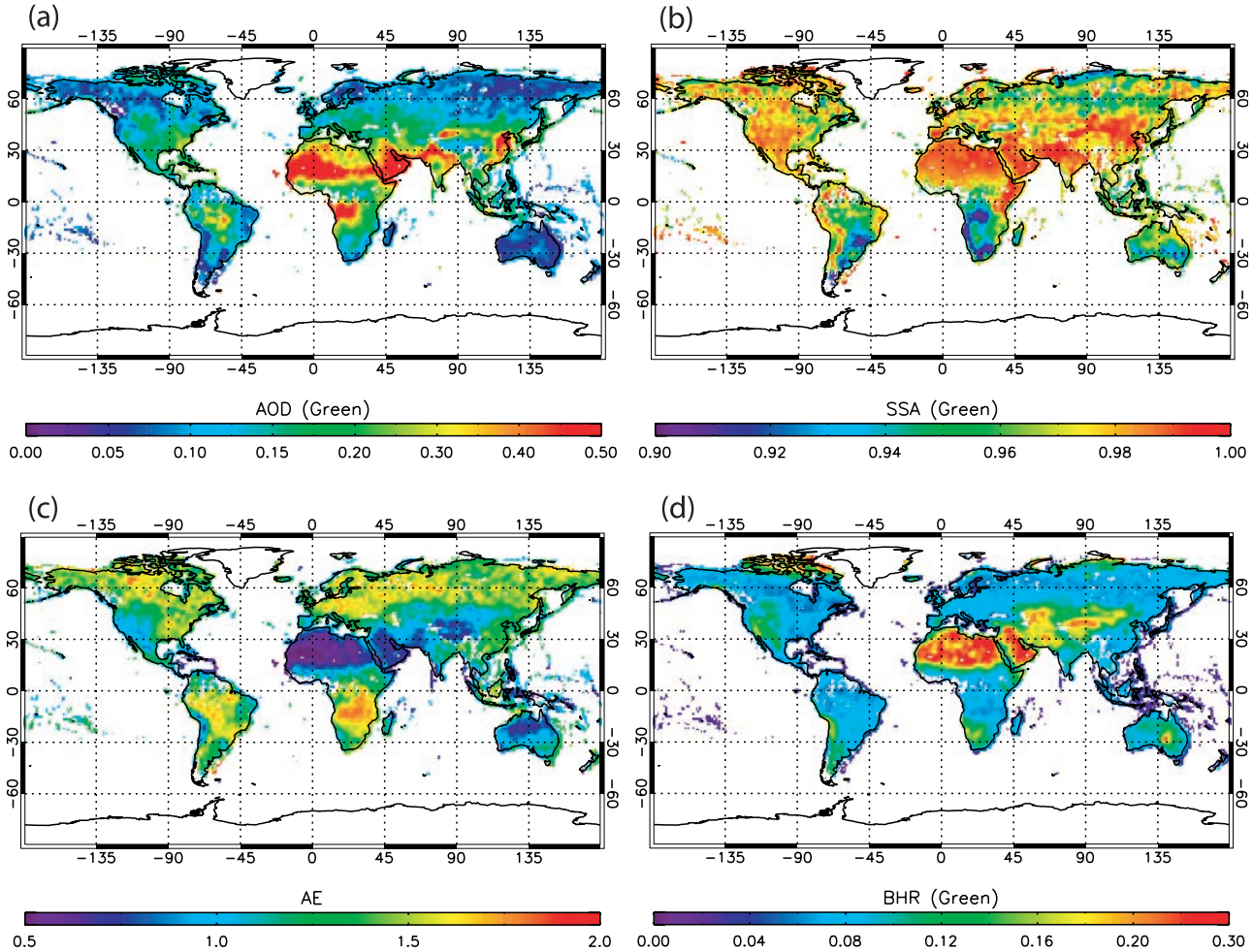

Figure 2. Global over-land distribution of MISR-observed (a) AOD, (b) SSA, (c) AE, and (d) surface BHR in cloud-free land region, averaged over June–September 2007, at 2° × 2° spatial resolution. The AOD, SSA, and BHR values shown are for the MISR green band (0.56 μm).

to affect the TOA albedo, was used for estimating $d\alpha$ when local linear regression failed. We prefer this method to simply putting missing data where linear regression fails on the basis of the following considerations. First, we attempted to provide a global average value of $d\alpha$. Since the probability of failure is usually larger over regions with small AODs, the simple average over successful regressions may result in a positively biased global mean value. Second, although the linear regression fails, the information on aerosol and surface properties may still be valid. We tried to utilize this information instead of discarding it.

3. Results

3.1. Global Distributions of Aerosol and Surface Properties Over Land

[22] The TOA albedo change due to the presence of aerosols in cloud-free regions is mainly determined by aerosol loading, aerosol optical properties, and surface reflectance. Figure 2 gives a global view of the 4-month (June–September 2007) mean MISR-retrieved AOD, SSA, AE, and surface BHR over land. The AOD, SSA, BHR values are for 0.56 μm (MISR green band). These values are averages for clear sky only. MISR-retrieved global mean values of AOD, SSA, BHR and AE over land are summarized in Table 2.

[23] High AOD values are seen in desert regions such as the Sahara and the Arabian Peninsula, in polluted regions including south and East Asia, eastern Europe, southeast United States, and in biomass burning regions such as central Africa and the Amazon (Figure 2a).

[24] Aerosol SSA, the ratio of scattering to total light extinction, indicates the relative importance of aerosol scattering versus absorption [*Bergstrom et al.*, 2003]. Figure 2b shows high SSA values (close to unity) in most industrialized and desert regions, where aerosol scattering dominates. Aerosols in biomass burning regions are more absorbing with smaller SSA values. In central Africa and South America, for example, averaged SSA values are as low as ~0.9, indicating relatively high aerosol absorption. This is also evident in Alaska, northern Canada and Siberia, where high AODs are correlated with low SSAs (see Figures 2a and 2b).

[25] The AE is inversely correlated with the average size of aerosol particles: the smaller the particles, the larger the exponent [*Angstrom*, 1929; *Schuster et al.*, 2006]. Small AE

Table 2. Mean Values of MISR Spectral AOD, SSA, AE, BHR, and Derived $d\alpha$ and Aerosol Radiative Efficiency Over Global Land and Over Each Vegetation Type for June–September 2007[a]

Parameters		Global Land	Needleleaf Forest	Broadleaf Forest	Shrub Land	Savanna	Grass Land	Crop Land	Barren
AOD	B	0.256 ± 0.051	0.124	0.241	0.176	0.248	0.225	0.271	0.404
	G	0.202 ± 0.040	0.091	0.184	0.135	0.182	0.174	0.204	0.343
	R	0.167 ± 0.033	0.070	0.148	0.120	0.140	0.143	0.161	0.303
	N	0.132 ± 0.026	0.051	0.112	0.085	0.101	0.113	0.120	0.261
SSA	B	0.964	0.964	0.953	0.963	0.955	0.974	0.972	0.974
	G	0.971	0.966	0.963	0.968	0.958	0.981	0.976	0.984
	R	0.974	0.967	0.968	0.971	0.958	0.984	0.978	0.989
	N	0.973	0.964	0.965	0.971	0.955	0.985	0.977	0.990
AE		1.170	1.413	1.222	1.228	1.373	1.115	1.356	0.845
BHR	B	0.067	0.043	0.054	0.067	0.051	0.068	0.054	0.114
	G	0.103	0.063	0.057	0.105	0.077	0.117	0.086	0.202
	R	0.120	0.044	0.041	0.122	0.082	0.139	0.079	0.285
	N	0.246	0.215	0.185	0.245	0.239	0.272	0.286	0.340
$d\alpha$	B	0.018 ± 0.003	0.0088	0.0178	0.0121	0.0164	0.0180	0.0236	0.0204
	G	0.010 ± 0.003	0.0039	0.0104	0.0067	0.0097	0.0105	0.0128	0.0130
	R	0.007 ± 0.003	0.0021	0.0071	0.0045	0.0072	0.0073	0.0080	0.0093
	N	0.008 ± 0.006	0.0025	0.0060	0.0046	0.0063	0.0063	0.0063	0.0170
Aerosol radiative efficiency	B	0.070	0.093	0.097	0.091	0.090	0.106	0.119	0.068
	G	0.048	0.037	0.052	0.043	0.046	0.057	0.058	0.041
	R	0.039	0.020	0.034	0.028	0.031	0.037	0.032	0.030
	N	0.052	0.027	0.029	0.031	0.031	0.033	0.028	0.046

[a]The values are given for MISR blue (B), green (G), red (R), and near-infrared (N) bands. Uncertainties are provided when available. Uncertainties for MISR spectral AOD are calculated by 20% × AOD on the basis of work by *Kahn et al.* [2005]. Uncertainties of dα are from this study. Absolute uncertainties for SSA, AE, and BHR are not yet known, owing to the difficulty in obtaining validation data.

values in desert regions (Figure 2c) are consistent with the presence of large dust particles. Large values of AE are observed over biomass burning and industrial regions where fine-mode aerosols dominate.

[26] Previous studies have shown that the fraction of energy reflected at a particular wavelength varies with surface type [e.g., *Kaufman et al.*, 2002b]. The MISR-derived BHR data shown in Figure 2d illustrates that global land surface is very heterogeneous in reflecting solar radiation. The less the vegetation cover, the larger the BHR values usually are in areas with high soil albedo. The largest BHR values are in desert and barren regions. The spectral signatures over different surface types have been observed to be very different [e.g., *Tucker and Sellers*, 1986]. For example, the reflectance over sand and soil increases with wavelength in the visible-NIR range, and the rate of increase diminishes at longer wavelengths. Over dense vegetation, the reflectance in the visible region is relatively uniform over the spectrum, with slightly higher values in the green band. From visible bands to NIR, however, there is a large jump in surface reflectance, known as the red–far red edge. These spectral signatures of surface types are well captured by MISR observations (Table 2 and Figure 2d). In vegetated regions, much higher BHR values are observed in the NIR band than visible bands, whereas in desert and barren areas, the BHR increases smoothly from the blue to the NIR band.

[27] The probability distributions of MISR AOD, SSA, BHR and AE over land are shown in the diagonal cells in Figure 3. Figure 3, cell B, shows that AOD has a narrower distribution at longer wavelengths. Most BHR values in visible bands are below 0.2, whereas in the NIR band, a peak near 0.3 is present (Figure 3, cell C). Most SSA distributions are above 0.9, with more small values in blue and green bands (Figure 3, cell D). AE values are mostly distributed between 0.5 and 2, with a broad peak at ~1.2 (Figure 3, cell E). The other cells of Figure 3 will be analyzed further in section 3.3.1.

3.2. TOA Albedo Change by Aerosols Over Land

[28] On the basis of linear regressions between the MISR TOA albedo and AOD, we estimate the aerosol effect on TOA albedo in the four MISR spectral bands. Figure 4 shows the 4-month (June–September 2007) mean spatial distributions of TOA albedo change due to the presence of aerosols ($d\alpha$) over cloud-free land. Persistent cloud cover over the Amazon, central Africa, Southeast Asia, and west Canada prevents MISR from observing enough cloud-free data to meet our criteria, so $d\alpha$ values over some portion of these regions are missing.

[29] The global means of $d\alpha$ over cloud-free land are 0.018 (blue), 0.010 (green), 0.007 (red), and 0.008 (NIR). We would expect $d\alpha$ to be large where AOD is high, especially if the aerosols are bright (high SSA) and reside over dark surfaces. We examine first the relationship between $d\alpha$ and AOD and then the relative contributions of surface and aerosol optical properties to $d\alpha$.

[30] The $d\alpha$ patterns show some similarity with the AOD pattern (Figure 2a); that is, high $d\alpha$ values are found in most high-AOD regions, including East Asia, the Indian and Arabian peninsulas, western Sahara, east Europe, and North America. However, high AOD is not always accompanied by high $d\alpha$. In some biomass burning regions with relatively small SSA (e.g., central Africa, see Figure 2b), $d\alpha$ is small owing to aerosol absorption. Small $d\alpha$ is also observed over bright surfaces, such as in northeastern Sahara, and in the desert regions of Australia and southern Africa.

[31] *Patadia et al.* [2008] neglected a large area spanning northern Africa to middle Asia in their calculation owing to inconsistent AOD-flux relations over high-reflectance surfaces. The use of internally consistent data sets and BHR

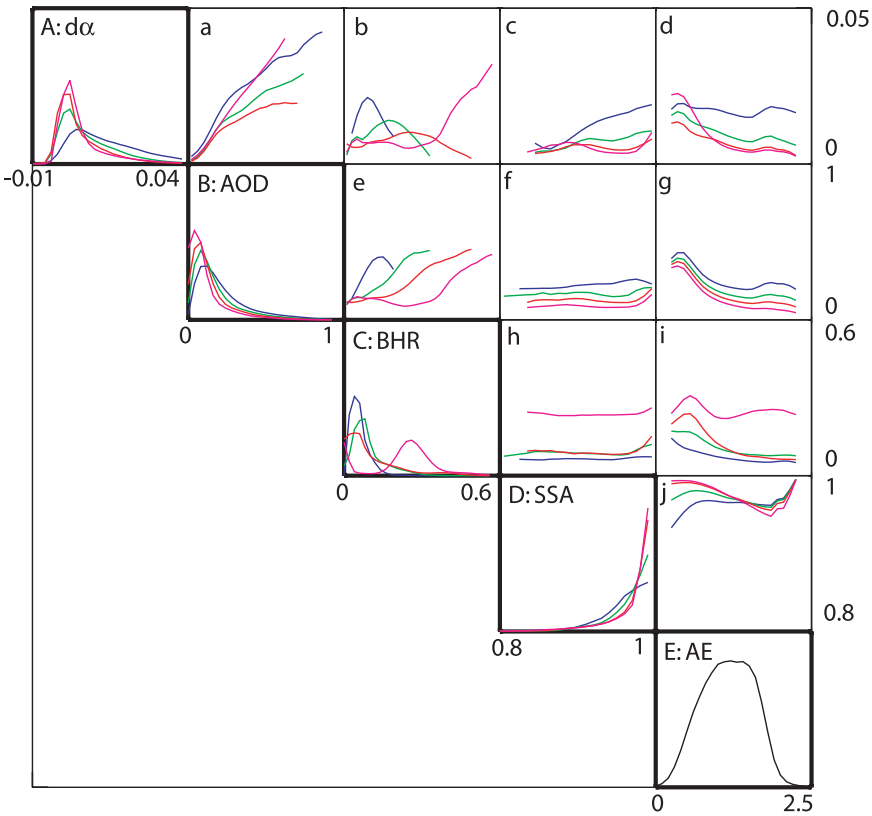

Figure 3. Probability distributions of $d\alpha$, AOD, BHR, SSA, and AE over global land are shown in diagonal cells (A–E). Also shown are fitted lines on the pairwise scatterplots of these variables (cells a–j). All cells are based on mean values of these variables in 2° × 2° regions during June–September 2007. Colored lines correspond to the four spectral bands (purple for NIR).

stratification in our study produces relatively good correlations between AOD and TOA albedo for this area. The inclusion of these high-reflectance regions, which account for about 10% of Earth's landmass, is necessary to accurately estimate the global aerosol radiative effect. Large aerosol loading (Figure 2a) and intense solar radiation (due to high sun at low latitude and low subtropical cloud cover) have the potential to cause a large aerosol radiative effect in these regions (Figure 4). We estimate that neglecting of these regions would produce an underestimate of global mean $d\alpha$ over land by ~5% of its value.

[32] In Figure 4, the detailed patterns of TOA albedo change due to aerosols over the Saharan desert and Arabian Peninsula demonstrate the value of our approach over bright surfaces. The aerosol effect on TOA albedo differs between the western and eastern parts of the highly reflective Saharan desert. In the western Sahara, aerosol loading is very high (mean AOD is greater than 0.5 at 0.56 μm wavelength; see Figure 2a), and small AE values (Figure 2c) are consistent with the single dominant aerosol component being large dust particles. The $d\alpha$ value in this part is also high (>0.03 at 0.56 μm). In northeastern Sahara, aerosol loading is much smaller, and the surface reflectance is higher. Relatively higher AE values suggest smaller aerosol size distributions, which could be due to the change in size distribution during dust transport, or different surface properties producing different mineral dust size distributions. Other sources of aerosols, such as pollution, may also contribute to the presence of small particles. The calculated $d\alpha$ in this region is clearly smaller than that in the western Sahara. Because the surface and dust particles have similar ability to reflect solar radiation, and also because the dust particles are weakly absorbing, negative values of $d\alpha$ (corresponding to a warming effect) are sometimes found in this region. For the southern rim of the Sahara, where a large dust burden occurs over a less reflective surface, $d\alpha$ is largest. There is a similar spatial distribution of $d\alpha$ in the Arabian Peninsula, with large values over darker surfaces in the western part near the Red Sea.

3.3. Dependence of $d\alpha$ and Aerosol Radiative Efficiency on Surface Reflectance and Aerosol Optical Properties

[33] Latitudinal distributions of spectral $d\alpha$ and MISR AOD at 0.56 μm are shown in Figure 5a. The $d\alpha$ generally decreases from the blue band to red band. The decrease is partly due to the smaller aerosol scattering at longer wavelength, and partly due to increasing surface reflectance from blue to red for most surface types (Table 2), which reduces the contrast between aerosol and the surface. The $d\alpha$ patterns for red band and NIR are similar.

[34] As in Figure 4, the $d\alpha$ distribution generally follows the AOD distribution, with two peaks located in 10°N–30°N and 0°–10°S (see also Figure 2a). However, there are some regions where the $d\alpha$ and AOD distributions do not match one another. For example, $d\alpha$ in the three visible

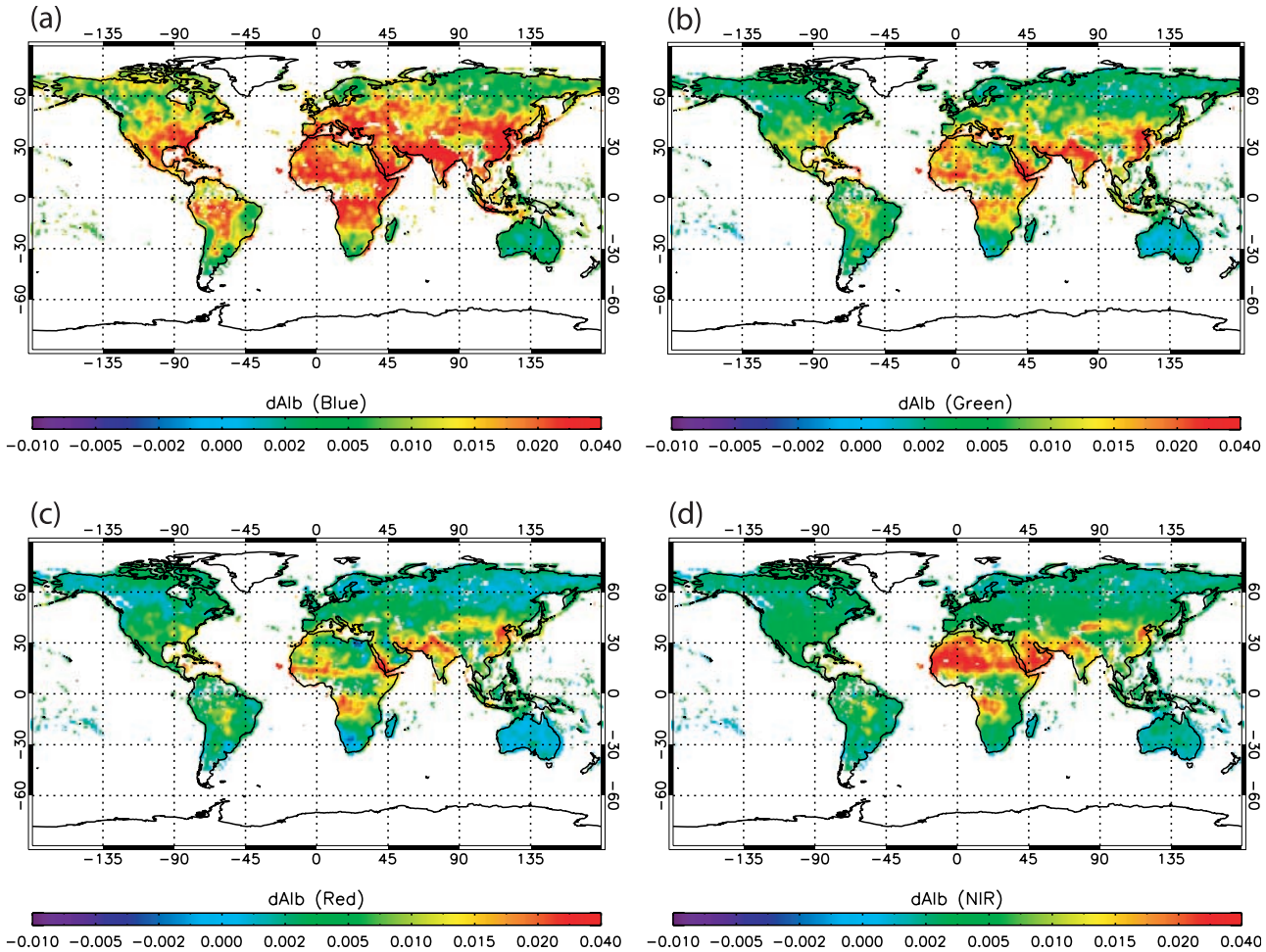

Figure 4. Global distribution of TOA albedo change by aerosols ($d\alpha$) in the four MISR bands: (a) blue, (b) green, (c) red, and (d) NIR, over cloud-free land regions, averaged over June–September 2007, at $2^\circ \times 2^\circ$ spatial resolution.

bands decreases from 10°N to 20°N despite the increase in AOD.

[35] In order to interpret these results, we introduce the concept of aerosol radiative efficiency. The aerosol radiative efficiency is defined here as $d\alpha$ normalized with respect to MISR AOD at 0.56 μm. It represents the aerosol's ability to change the TOA albedo. The latitudinal distributions of spectral aerosol radiative efficiencies, together with the MISR-retrieved surface and aerosol properties (BHR and SSA at 0.56 μm, and AE), are shown in Figure 5b. The aerosol radiative efficiencies have very different latitudinal distributions from the $d\alpha$ distributions but are directly linked to the distributions of aerosol and surface properties. The two dips near 20°N and 30°S are likely due to the large BHR in those regions (also shown in Figure 2d). From 10°N to 20°N, the aerosol radiative efficiency decreases abruptly in the visible bands owing to the increase of BHR, which explains why $d\alpha$ decreases despite the increase in AOD (Figure 5a). In other regions where surface reflectance is low, the aerosol radiative efficiency is positively correlated with SSA. From 30°S to 40°S, both the increase of SSA and the decrease of BHR contribute to a significant rise in the aerosol radiative efficiency. The largest efficiency is in the midlatitude Northern Hemisphere, where the vegetation cover is dense so the surface reflectance is small (see Figure 2d), and the aerosol particles are generally small (see Figures 2c and 5b) and highly scattering (see Figures 2b and 5b).

[36] The patterns shown in Figures 4 and 5 clearly indicate that the TOA albedo change by aerosols, $d\alpha$, is influenced not only by the aerosol radiative properties, but also by surface reflectance. We explore the dependence of $d\alpha$ and aerosol radiative efficiency on surface reflectance and aerosol optical properties in more detail, including AOD, SSA, and AE dependencies.

3.3.1. The $d\alpha$

[37] In addition to the probability distribution functions for each variable, discussed above, Figure 3 gives the correlations between calculated $d\alpha$ and MISR AOD, BHR, SSA, and AE. Fitted lines for correlations between each pair of these variables are plotted in cells above the diagonal, on the basis of statistics on all $2^\circ \times 2^\circ$ grid cells over land, for June–September 2007.

[38] In general, $d\alpha$ increases, albeit nonlinearly, with increasing AOD (hence larger aerosol scattering) for all four spectral bands (Figure 3, cell a). The slopes are largest

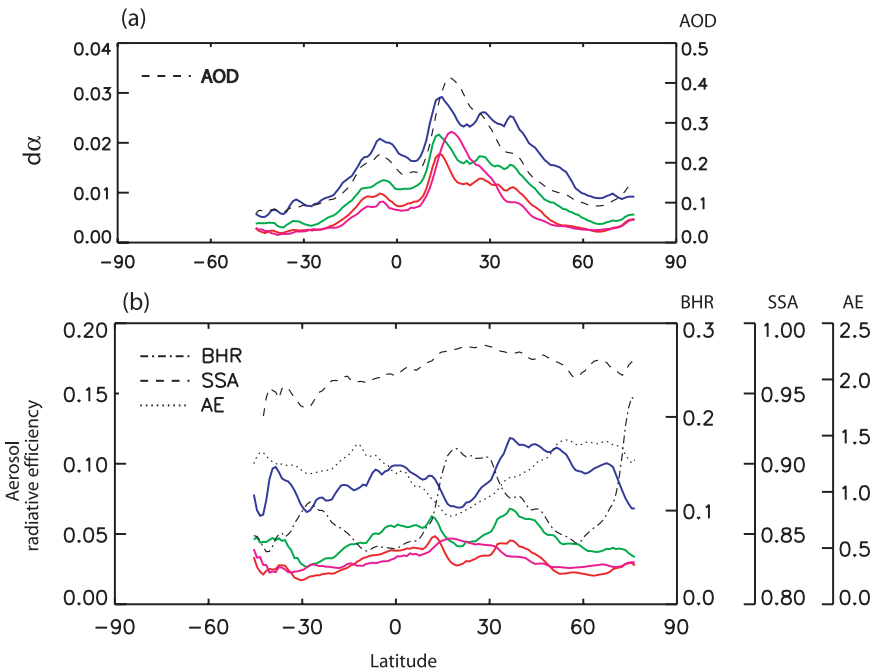

Figure 5. Latitudinal distributions of (a) $d\alpha$ and (b) aerosol radiative efficiency in four spectral bands: blue (blue line), green (green line), red (red line), and NIR (purple line). The distribution of MISR AOD (0.56 μm) (black dashed line in Figure 5a) and BHR (0.56 μm), SSA (0.56 μm), and AE (black lines in Figure 5b) are also shown. These data are averaged over June–September 2007.

in the blue band where the largest aerosol radiative efficiencies occur (see Figure 5b). The slopes tail off at larger AOD values (~0.2). This may be partly explained by aerosol multiscattering at higher aerosol loading [*Bissonnette*, 1988]. Additionally, brighter surfaces with higher BHR values, where AOD values are typically large (Figure 3, cell e), tend to decrease the aerosol radiative efficiency.

[39] The dependence of $d\alpha$ on surface reflectance is complex. Figure 3, cell b, shows that when BHR is small, the correlation between $d\alpha$ and BHR is weak. When BHR is higher, $d\alpha$ starts to increase with increasing BHR. This pattern can be attributed to the correlation between AOD and BHR (Figure 3, cell e), which shows AOD increases with increasing BHR when BHR is large enough. In this regime, the increase in AOD apparently outweighs the decrease of aerosol radiative efficiency caused by increasing BHR (as shown in Figure 5b). When BHR is very large, as shown in Figure 3, cell e, the correlation between AOD and BHR is weak again. In this regime, the increased BHR dominates, leading to decreased aerosol radiative efficiency and smaller slope of $d\alpha$–BHR.

[40] Many studies emphasize the importance of SSA, which represents the relative contributions of aerosol scattering and absorption, in affecting the Earth-atmosphere radiation budget [e.g., *Hansen et al.*, 1998]. Aerosols with large SSA scatter the incoming solar radiation, cooling the atmosphere and surface. For fixed AOD, the net effect of increasing aerosol absorption (lowering SSA) is to decrease TOA albedo, owing to the absorption. Figure 3, cell c, demonstrates this $d\alpha$ decrease with decreasing SSA, an effect that is more obvious for blue and green bands. For the majority of the SSA range, the change in AOD and BHR with changing SSA is small (Figure 3, cells f and h). Therefore, the positive correlation of $d\alpha$ and SSA is mainly caused by the change SSA makes to the aerosol radiative efficiency. Figure 3, cell c, also shows that the spectral difference of $d\alpha$ is largest at high SSA. The spectral difference becomes much smaller when aerosol absorption is important (i.e., SSA is low). This dependence pattern is also seen in Figure 4, which shows the largest $d\alpha$ change from the blue to NIR bands in industrial and desert regions, where SSA is high (Figure 2b). We also notice that when SSA is close to unity, positive correlations between AOD and SSA are present (Figure 3, cell f), which additionally increases the slope of $d\alpha$–SSA (Figure 3, cell c).

[41] In general, AE is inversely related to the aerosol size. The relationship between $d\alpha$ and AE (Figure 3, cell d) can be explained by the correlations between AE and other aerosol and surface properties (AOD, BHR, and SSA). Over the majority of the AE range (0.5–2.0, as shown in Figure 3, cell E), $d\alpha$ decreases with increasing AE, mainly because of the negative correlation between AOD and AE (Figure 3, cell g). Because BHR also decreases with increasing AE (Figure 3, cell i), the slopes of $d\alpha$–AE are smaller than those of AOD–AE. Figure 3, cell j, shows SSA is also inversely correlated to AE when aerosol size is in the moderate range. Strong light absorption (low SSA) is mainly associated with small particles (AE-2 as shown in Figure 3, cell E). However, small SSA values when AE-0 indicate that very large particles may also absorb light in the blue and green bands. Figure 3, cell j, shows that typically, SSA decreases with wavelength for small particles (AE > ~1.5), but increases with wavelength for large particles. This is consistent with previous aircraft measurements [*Bergstrom et al.*, 2002]. The different spectral dependence of SSA in the MISR products is a consequence of the particle models

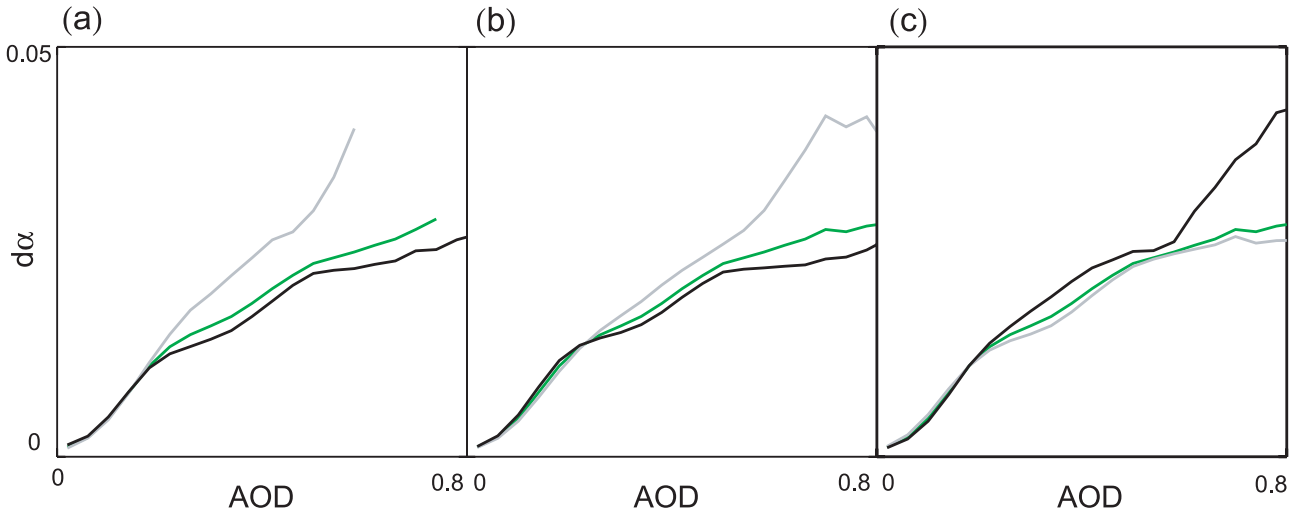

Figure 6. (a) Dependence of $d\alpha$–AOD correlations on BHR in the green band. Grey line is the fitted line on correlation between $d\alpha$ and AOD for data sets with small BHR (smaller than the median of all BHR values in $2^\circ \times 2^\circ$ regions globally). Black line represents the correlation for data sets with large BHR (larger than median). Green line is fitted line for the whole data set. (b) Similar to Figure 6a, except for small and large SSA. (c) Similar to Figure 6a, except for small and large AE.

underlying the MISR aerosol retrievals and is based on a combination of satellite-measured radiances and prior knowledge from field observations [e.g., *Kahn et al.*, 2001].

[42] Figure 6 demonstrates how the $d\alpha$ dependence on AOD is affected by BHR, SSA and AE (in the green band). The rate of increase of $d\alpha$ with AOD is smaller when BHR is larger. The decreased rate is significant only when AOD is larger than ~0.2. For higher AOD, this difference becomes larger. As might be expected, the $d\alpha$–AOD correlation slope is larger also for brighter (higher SSA) particles. However, the increase in slope is smaller for higher SSA, and is less dramatic than the AOD dependence. Probably owing to weak inverse correlation between BHR and AE (Figure 3, cell i), the $d\alpha$–AOD slope is higher when AE is larger.

3.3.2. Aerosol Radiative Efficiency

[43] To further illustrate the dependence of $d\alpha$ on aerosol properties and surface reflectance, we plot the aerosol radiative efficiency as a function of BHR, SSA, and AE in Figure 7. Because there are not enough data points, lines in Figure 7a stop at certain BHR values. Figure 7a shows that aerosol radiative efficiencies do not change substantially with BHR when the surface is dark (low BHR). When the surface is brighter (i.e., BHR surpasses a critical value), the aerosol radiative efficiencies decrease as BHR increases. This relationship causes a strong correlation between aerosol radiative efficiency and BHR when BHR is large, as shown in Figure 5b. Figure 6a also shows the critical BHR value increases with wavelength, and the slope becomes smaller for longer wavelength.

[44] The positive correlation between aerosol radiative efficiency and SSA (Figure 7b) is similar to that between $d\alpha$ and SSA (Figure 3, cell c). For blue and green bands, the radiative efficiency increases with increasing SSA. This correlation contributes to the agreement between the aerosol

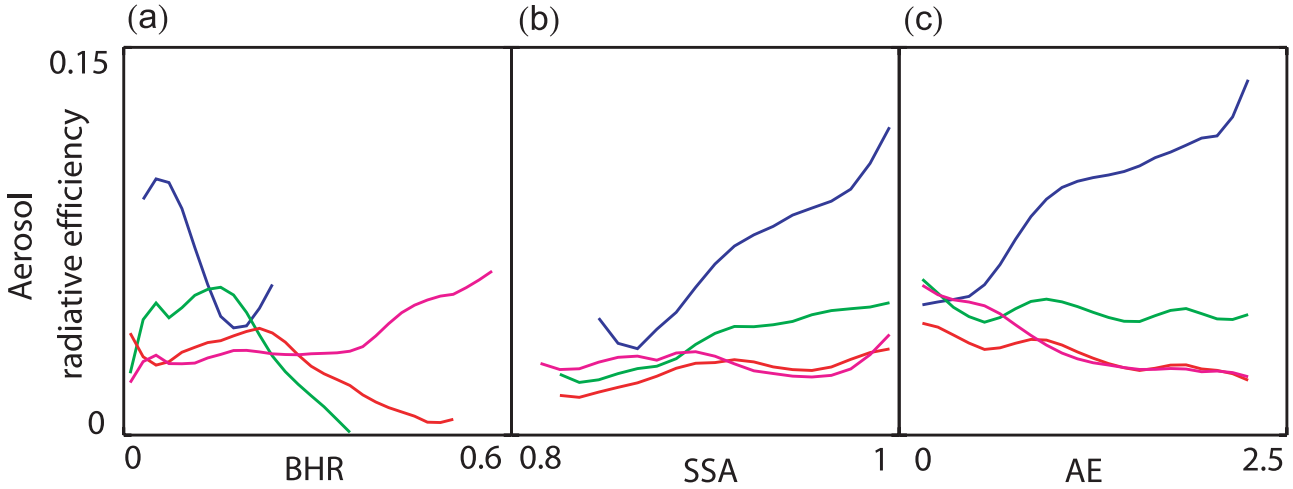

Figure 7. Aerosol radiative efficiency versus BHR, SSA, and AE in four spectral bands.

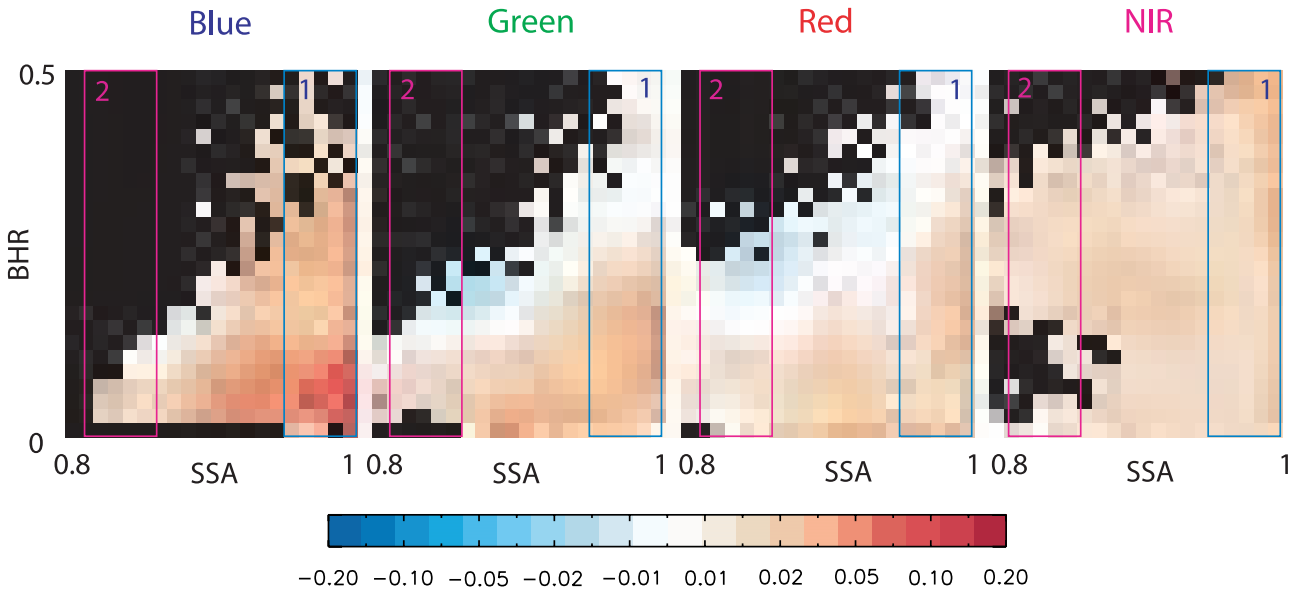

Figure 8. Aerosol radiative efficiencies versus BHR and SSA in four spectral bands. Red means that the aerosols increase the TOA albedo, while blue indicates the aerosol effect on TOA albedo is negative. Box 1 and box 2 represent cases with high SSA and low SSA, respectively.

radiative efficiency pattern and the SSA pattern (Figure 5b) outside the high-BHR region.

[45] The dependence of aerosol radiative efficiency on AE (Figure 7c) can be attributed to the combined effect of the BHR-AE correlation (Figure 3, cell i) and the SSA-AE correlation (Figure 3, cell j). For the blue band, BHR decreases and SSA increases with increasing AE. Both effects contribute to the increase of aerosol radiative efficiency. For the NIR band, the correlation between BHR and AE is weak. The negative correlation between aerosol radiative efficiency and AE is mainly determined by the SSA-AE relationship. For the green and red bands, the two effects nearly cancel out and the aerosol radiative efficiencies are not sensitive to AE.

[46] We should bear in mind that since BHR is predominantly a surface property, the above-mentioned empirical correlation of BHR with aerosol properties may not represent a simple causal relationship. However, some connections are likely, such as bright desert surfaces being the source for bright, and relatively high AOD, airborne mineral dust.

3.3.3. Effect of Surface Reflectance on Aerosol Scattering and Absorption

[47] As discussed above, the increasing of TOA albedo by aerosol scattering and the decreasing by aerosol absorption together determine the aerosol radiative efficiency. Figure 8 illustrates how the change of surface reflectance mediates the influence of aerosol scattering and absorption. The derived aerosol radiative efficiencies for all $2^\circ \times 2^\circ$ grid cells globally are stratified on the basis of their BHR and SSA values, and the mean aerosol radiative efficiency is shown for each stratum.

[48] Figure 8 helps to additionally separate the contributions from BHR and SSA. When SSA is close to 1 (box 1 within each spectral panel in Figure 8), the dominant effect is aerosol scattering. When the surface is brighter, the net downwelling shortwave radiance passing through the atmosphere is smaller, because the surface reflects more radiance back to the space. In other words, the contrast between the reflectance from aerosols and surface is smaller. This effect decreases the magnitude of TOA albedo change by aerosols. As a consequence, as shown in box 1 of Figure 8, the aerosol radiative efficiencies decrease with increasing BHR for blue, green, and red bands. It is less obvious for NIR.

[49] When SSA is small, the contribution from absorptive aerosols changes the aerosol radiative efficiency, as well as its dependence on surface reflectance. By using a radiative transfer model, *Satheesh* [2002] showed that for a given aerosol system, the effect of soot absorption is significantly larger over brighter surface (either land or clouds) because the radiation reflected from the surface below would interact with the aerosols again. Our results in Figure 8 (box 2) show such an enhancement as well. As BHR increases, the aerosol radiative efficiency (for constant SSA) decreases, and turns negative when BHR exceeds a certain threshold. The presence of cases with negative values indicates that aerosols may warm the atmosphere when the surface is highly reflective. The amplification effect is especially true for the green and red bands.

3.4. The $d\alpha$ Patterns Over Different Vegetation Types

[50] Vegetation cover determines the ratio of reflection and absorption of solar radiation by the land surface. Knowing the TOA albedo change by aerosols over different vegetation types will help establish how land cover change, such as desertification and deforestation, will alter the aerosol radiative effect. Land cover change may be accompanied by the change of aerosol optical properties, owing to the alteration of biogenic emissions, biomass burning, or industrial activities. But on short timescales, we can assume the aerosol optical properties remain unchanged after a change in vegetation type. MODIS provides a 1-km land cover product (MOD12Q1), which includes an IGBP (International

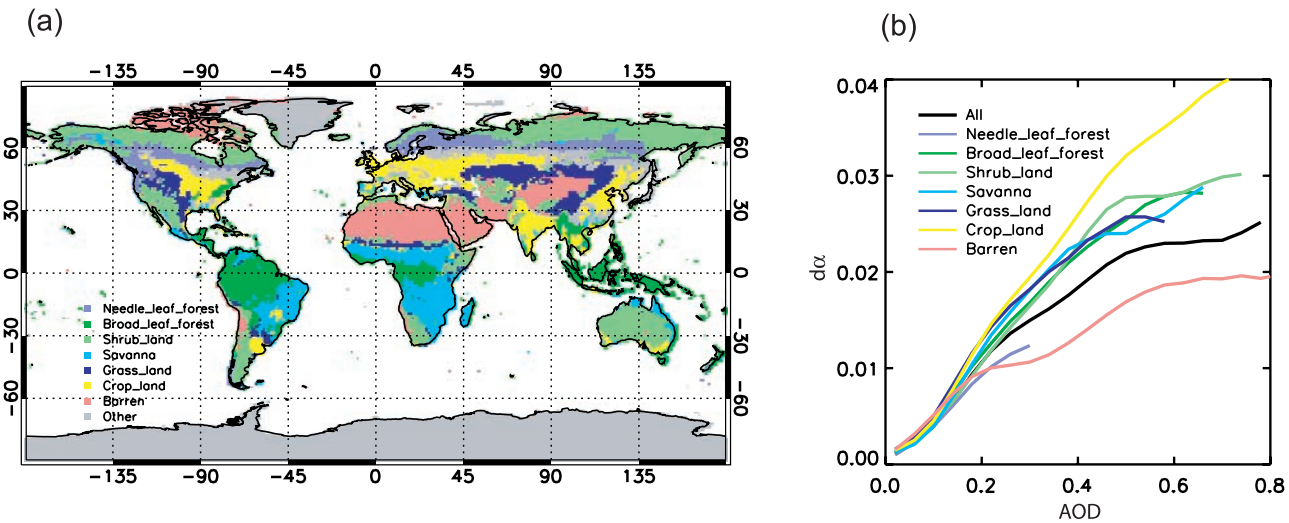

Figure 9. (a) Global map of aggregated vegetation types derived from annual mean MODIS land cover product. (b) Calculated $d\alpha$ versus AOD in the green band (0.56 μm) over different vegetation types. The black line shows the globally averaged values over all vegetation types.

Geosphere-Biosphere Programme) land cover classification map of the globe [*Belward et al.*, 1999; *Scepan et al.*, 1999]. We aggregated the MODIS land cover into seven land vegetation types, covering regions where enough land area and sample size are available: needleleaf forest, broadleaf forest, shrubland, savanna, grassland, cropland, and barren areas. The dominant surface type in each 2° × 2° grid cell was determined and is shown in Figure 9a.

[51] Correlations between blue band $d\alpha$ and AOD over different vegetation types are shown in Figure 9b. Compared to other surface types, barren regions have the lowest slope, indicating aerosols over these regions have the smallest radiative efficiency. Most barren regions are located at 15°N–30°N (see Figure 9a), where high surface reflectance (Figures 2d and 5b) reduces the aerosol effect on TOA albedo. However, because the aerosol loading over these regions is generally high (Figure 2a and 5a), the mean $d\alpha$ is still large (see Table 2). Figure 9a shows the southern edge of the Sahara desert to be adjacent to grassland and savanna ecosystems, which have much smaller $d\alpha$–AOD slope (Figure 9b). Owing to this large contrast, the $d\alpha$ in this region has a large gradient (Figure 4b).

[52] Figure 9b also shows the largest dependence of $d\alpha$ on AOD is over croplands, which are mainly located near the industrial regions of the Northern Hemisphere, such as East and south Asia, Europe, and eastern Unites States (Figure 9a). For a majority of these regions, the SSA value is large (Figure 2b) and BHR is small (Figure 2d), which both contribute to large aerosol radiative efficiency (30°N–60°N in Figure 5b). In addition, these regions have moderate to large AOD (Figure 2a), likely due to anthropogenic emissions. All these factors make croplands the vegetation type with largest $d\alpha$ (Table 2).

[53] Over most forests and grasslands, the correlations between $d\alpha$ and AOD are similar (Figure 9b), which means the aerosol radiative efficiency would be similar given similar AOD distributions. However, because aerosol loading over needleleaf and shrublands is small (Table 2), the aerosol radiative efficiency and $d\alpha$ in these regions are small.

[54] The mean values of $d\alpha$ over different land vegetation types in all four MISR spectral bands are summarized in Table 2. A decrease of $d\alpha$ from short wavelength (blue band) to long wavelength (NIR) is seen for most vegetation types. Overall, the smallest $d\alpha$ values are over needleaf forests and shrublands, whereas the largest values are over cropland and barren regions. The aerosol radiative efficiencies are lowest over needleleaf forest and barren regions, and highest over grasslands and croplands.

4. Uncertainty

[55] In this study, we use the MISR TOA albedo product and aerosol properties to derive the aerosol effect on TOA albedo. The availability of good quality AOD makes it possible to derive aerosol radiative effect over bright land surfaces. We also use MISR BHR to stratify the surface, which decouples the effects contributed by aerosols and surface. Despite these improvements, both unbiased and biased uncertainties still exist in the current estimation of TOA albedo change by aerosols. In this study, we consider three types of uncertainties: the uncertainty from the linear regressions, the uncertainty from the intrinsic scatter of MISR retrieved data, and the uncertainty due to cloud contamination.

[56] In the present study, the y intercept of the TOA albedo–AOD linear regression is assumed to be the aerosol-free TOA albedo. *Isobe et al.* [1990, equation (9)] provide an approach for calculating the variance of the intercept from a linear regression. On the basis of this approach, we estimate the variance of $d\alpha$ for each linear regression. When the regression is not successful, $d\alpha$ is estimated from the mean AOD and a predetermined scaling factor that depends on the mean SSA and BHR values for the region, as described in section 2.2. Since the derivation of this scaling factor is based on the slopes (b) of all available successful regressions, we simply assume the variance of the scaling factor is twice the mean variances of slopes. The variance of the slope (b) for each successful regression is also derived

using the method of *Isobe et al.* [1990]. For each 2° × 2° grid cell, the mean variance of $d\alpha$ is the sample-number-weighted mean variance of $d\alpha$ for every BHR set, including successful and unsuccessful regressions. By assuming the variance of $d\alpha$ is uncorrelated over different regions, we estimate the overall error due to the linear regression derived from this study is 0.0013 (blue), 0.0012 (green), 0.0015 (red), and 0.0019 (NIR).

[57] The uncertainty of $d\alpha$ also results from the intrinsic uncertainty of MISR retrieved AOD and TOA albedo. By comparing a 2-year measurement record of globally distributed AERONET Sun photometers, *Kahn et al.* [2005] showed that about 1σ of the MISR-retrieved AOD values fall within ±0.05 (or 20%) of AERONET. Here we use 20% as the uncertainty range of global mean AOD in all four bands. By multiplying this uncertainty by the mean slope of the TOA albedo−AOD relationship (~0.04 per unit of AOD), we obtain an additional uncertainty of 0.002 in the global mean $d\alpha$. The radiometric uncertainty of MISR radiances due the calibration is about 3–4% [*Bruegge et al.*, 2007]. In the MISR retrieval, top-leaving radiances were integrated either using an azimuthal model (AZM) or a Solid Angle Weighting method for cloud-free scenes. There are uncertainties in determining the integration coefficients for either method [*Diner et al.*, 1999]. The standard deviation of the albedo values with the AZM approach has been evaluated for different surface types in cloud-free scenes. Most albedo errors lie between 1% and 2% [*Diner et al.*, 1999; *Sun et al.*, 2006]. So we estimate the uncertainty of $d\alpha$ caused by the intrinsic uncertainty in MISR retrieved TOA albedo to be 4% × $\overline{d\alpha}$, where $\overline{d\alpha}$ is the global mean of the TOA albedo change by aerosols. We estimate global mean of this uncertainty to be 0.00072 (blue), 0.0004 (green), 0.00028 (red), 0.00032 (NIR).

[58] Another source of uncertainty results from the use of a cloud mask to distinguish the cloudy from the cloud-free regions. Although we use stringent cloud screening in this study to minimize the cloud effect (see section 2.1), occasional misclassification of cloudy region as cloud-free region will systematically introduce a high bias. Additionally, the neglect of partly cloud-covered regions may bias the results toward situations dominated by large high-pressure systems [*Remer and Kaufman*, 2006]. However, this source of uncertainty is difficult to quantify, owing to the scarcity of relevant studies. To estimate this uncertainty, we used two independent cloud mask products derived from MISR observations (SVM Cloud Confidence Level and the Cloudy Clear Designator). We also tried looser and more stringent ways of aggregating the cloud masks to 17.6 × 17.6 km^2 resolution. We find that the global mean $d\alpha$ varies by 0.0015 (blue), 0.0012 (green), 0.0020 (red), 0.0051 (NIR) owing to the use of different cloud masks.

[59] If we assume the uncertainties from different sources are uncorrelated, the total variance is the sum of variances from all the above mentioned sources. On the basis of this calculation, the total uncertainty of global mean $d\alpha$ in this study is estimated to be 0.0029 (blue), 0.0027 (green), 0.0032 (red), 0.0058 (NIR). By neglecting the diurnal and seasonal cycle, this corresponds to an uncertainty in clear-sky aerosol SWDRE of ~1.2 W/m^2.

[60] However, regional uncertainties could be higher, and additional bias errors may exist. For example, in regions with large spatial variability of aerosol and surface properties, the correlations between TOA albedo and AOD are generally small and the $d\alpha$ uncertainty is high. Over desert regions where surface reflectance is high, the aerosol retrievals may contain some information from the surface, causing an overestimation of the aerosol radiative effect. The lack of small AOD values (particularly in the NIR band) may bring on additional uncertainty to the linear regression (small perturbation at high AOD may cause large variation in retrieved intercept). The regressions could also deteriorate when persistent cloud cover is present so that the total number of data samples is small. It should also be noted that uncertainties contributed by the regional correlations are not included in the present analysis.

5. Summary and Conclusions

[61] Despite recent major advances in atmospheric modeling and measurements, there is still large uncertainty in the estimation of the global aerosol radiative effect. Particularly, owing to the difficulty of retrieving AOD over bright land surfaces, satellite-based estimation of aerosol radiative effect over such surfaces is still missing [*Yu et al.*, 2006]. Another major challenge is owing to the highly heterogeneous nature of land surface types. The study presented in this paper demonstrates how internally consistent MISR aerosol, albedo, and surface observations can be used to assess the aerosol effect on TOA albedo over global land. More importantly, by using more reliable MISR AOD and aerosol properties over bright land surfaces, and BHR stratification to decouple aerosol and surface effects, this approach not only expands the spatial coverage, but also reduces the uncertainty in aerosol radiative effect estimates on global land.

[62] We have estimated the 4-month (June–September 2007) mean value of clear-sky TOA albedo change due to the presence of aerosols ($d\alpha$) over global land to be 0.018 ± 0.003 (blue), 0.010 ± 0.003 (green), 0.007 ± 0.003 (red), and 0.008 ± 0.006 (NIR). Major uncertainties originate from the linear regressions, the intrinsic scatter of MISR retrieved data, and cloud contamination. Individual regions show large spatial variability. Largest values of $d\alpha$ occur in the latitude bands 10°N–30°N and 0°–10°S. The mean $d\alpha$ at 0.56 μm over bright Saharan Desert and Arabian Peninsula is 0.015. Neglecting these areas would cause an underestimation of the mean value over global land by ~5%.

[63] The global patterns of $d\alpha$ are determined mainly by aerosol loading and surface reflectivity (BHR); aerosol radiative efficiency (defined as $d\alpha$ normalized by AOD at 0.56 μm) helps isolate the AOD contributions from other factors. In general, $d\alpha$ increases with increasing AOD, with increasing SSA, and with decreasing surface brightness, as expected. But the dependence of $d\alpha$ on AOD decreases at high AOD, possibly owing to a positive correlation between AOD and BHR. The slopes of $d\alpha$ also decrease with increasing particle size (i.e., with decreasing AE); the AE dependence is apparently due to its negative correlation with AOD.

[64] Aerosol radiative efficiency is influenced by the surface reflectance and SSA. When SSA is high, the dominant aerosol scattering effect increases the TOA albedo. Over bright (high BHR) surfaces, the added contribution of

aerosol scattering is less significant, which diminishes the aerosol radiative efficiency. When SSA is small and aerosol absorption is important, the TOA albedo change due to the presence of aerosols is also small, because absorbing aerosols reduce the radiance scattered back to space. This effect is enhanced over bright surfaces. In regions with high BHR and low SSA, the aerosol radiative efficiency can be negative; that is, aerosols may exert a warming effect on the atmosphere. The 4-month mean aerosol radiative efficiencies over global land derived from this study are 0.089 (blue), 0.050 (green), 0.035 (red), 0.040 (NIR).

[65] We also divided the global land surface into seven vegetation cover types and calculated the mean $d\alpha$ for each type. Despite the large surface reflectance, $d\alpha$ over barren regions is high owing to the large aerosol loading. The $d\alpha$ over global croplands is also high, attributed to the small BHR and large SSA. Smallest $d\alpha$ is over needleleaf forests and shrublands, where the aerosol loading is small.

[66] Aerosols affect the radiative balance in the atmosphere by modifying the TOA albedo. The $d\alpha$ calculated in this study is a first step toward to estimating aerosol broadband shortwave direct radiative effect (SWDRE). First, the change of spectral TOA albedo due to the presence of aerosols can be converted to the change of TOA broadband radiative flux. Second, since the Terra satellite which carries the MISR instrument is in a Sun-synchronous orbit, the current estimated $d\alpha$ is only an ''instantaneous'' value and a daily cycle albedo model must be applied to convert this value to daily mean value. A multispectral radiation transfer model will facilitate these conversions [e.g., *Kaufman et al.*, 2002b].

[67] The method presented in this paper can be extended to over ocean with some modifications. MISR BHR product is not available over ocean. Solar zenith angle, wind speed and ocean chlorophyll concentration are major factors affecting the ocean surface albedo [*Jin et al.*, 2004]. We can use these parameters to stratify the ocean surface and do similar regressions in each stratum. The detailed estimation of aerosol SWDRE over global land and ocean using MISR observations will be addressed in part 2 of this series. Additionally, direct aerosol forcing has to be extended into partly cloudy and cloudy regions. These regions are likely to have high TOA reflectances, and consequently small or negative values of $d\alpha$. Including these areas will decrease the aerosol SWDRE.

[68] The aerosol radiative effect estimated in this study includes contributions from both natural and anthropogenic aerosols. In addition to the composite aerosol amount and optical properties, MISR is also able to provide the aerosol optical depth stratified by aerosol types [*Kahn et al.*, 2001; *Kalashnikova and Kahn*, 2006; *Chen et al.*, 2008]. This aerosol climatology information, which will be recorded in a future MISR Level 3 Joint Aerosol Research Product, can be exploited to distinguish natural aerosol effect from anthropogenic influences. Following a similar approach as we used here, these data will make possible improved estimation of aerosol radiative forcing over land.

[69] **Acknowledgments.** This work is performed at the Jet Propulsion Laboratory, California Institute of Technology, under contract with NASA. The research of Y. Chen is funded in part by the NASA Earth Observing System MISR project, and in part by NASA grant 622-59-66-40. Q. Li is supported in part by the NASA Atmospheric Composition Modeling and Analysis program. The work of R. Kahn is funded in part by the NASA Earth Sciences Climate and Radiation and Atmospheric Composition programs, under H. Maring and P. DeCola, respectively, and in part by the MISR project. MISR data were obtained from the NASA Langley Atmospheric Sciences Data Center (http://www.eosweb.larc.nasa.gov).

References

Abdou, W. A., D. J. Diner, J. V. Martonchik, C. J. Bruegge, R. A. Kahn, B. J. Gaitley, K. A. Crean, L. A. Remer, and B. Holben (2005), Comparison of coincident MISR and MODIS aerosol optical depths over land and ocean scenes containing AERONET sites, *J. Geophys. Res.*, *110*, D10S07, doi:10.1029/2004JD004693.

Anderson, T. L., et al. (2005), An ''A-Train'' strategy for quantifying direct climate forcing by anthropogenic aerosols, *Bull. Am. Meteorol. Soc.*, *86*, 1785–1809.

Angstrom, A. (1929), On the atmospheric transmission of Sun radiation and on dust in the air, *Geogr. Ann.*, *11*, 156–166, doi:10.2307/519399.

Armston, J. D., P. F. Scarth, S. R. Phinna, and T. J. Danaher (2007), Analysis of multi-date MISR measurements for forest and woodland communities, Queensland, Australia, *Remote Sens. Environ.*, *107*, 287–298, doi:10.1016/j.rse.2006.11.003.

Belward, A. S., J. E. Estes, and K. D. Kline (1999), The IGBP-DIS global 1-km land-cover data set DISCover: A project overview, *Photogramm. Eng. Remote Sens.*, *1999*(9), 1013–1020.

Bergstrom, R. W., P. B. Russell, and P. Hignett (2002), Wavelength dependence of the absorption of black carbon particles: Predictions and results from the TARFOX experiment and implications for the aerosol single scattering albedo, *J. Atmos. Sci.*, *59*(3), 567–577, doi:10.1175/1520-0469(2002)059<0567:WDOTAO>2.0.CO;2.

Bergstrom, R. W., P. Pilewskie, B. Schmid, and P. B. Russell (2003), Estimates of the spectral aerosol single scattering albedo and aerosol radiative effects during SAFARI 2000, *J. Geophys. Res.*, *108*(D13), 8474, doi:10.1029/2002JD002435.

Betts, A. K., J. H. Ball, A. C. M. Beljaars, M. J. Miller, and P. A. Viterbo (1996), The land surface-atmosphere interaction: A review based on observational and global modeling perspectives, *J. Geophys. Res.*, *101*(D3), 7209–7225, doi:10.1029/95JD02135.

Bissonnette, L. R. (1988), Multiscattering model for propagation of narrow light beams in aerosol media, *Appl. Opt.*, *27*(12), 2478–2484.

Bruegge, C. J., D. J. Diner, R. A. Kahn, N. Chrien, M. C. Helmlinger, B. J. Gaitley, and W. A. Abdou (2007), The MISR radiometric calibration process, *Remote Sens. Environ.*, *107*, 2–11, doi:10.1016/j.rse.2006.07.024.

Charlson, R. J., J. Langner, and H. Rodhe (1990), Sulphate aerosol and climate, *Nature*, *348*, 22, doi:10.1038/348022a0.

Chen, W.-T, R. Kahn, W.-H. Li, and J. Seinfeld (2008), Sensitivity of multiangle imaging to optical and microphysical properties of biomass burning aerosols, *J. Geophys. Res.*, *113*, D10203, doi:10.1029/2007JD009414.

Christopher, S. A., and J. Zhang (2002), Shortwave aerosol radiative forcing from MODIS and CERES observations over the oceans, *Geophys. Res. Lett.*, *29*(18), 1859, doi:10.1029/2002GL014803.

Christopher, S. A., J. Chou, J. Zhang, X. Li, T. A. Berendes, and R. M. Welch (2000), Shortwave direct radiative forcing of biomass burning aerosols estimated using VIRS and CERES data, *Geophys. Res. Lett.*, *27*, 2197–2200, doi:10.1029/1999GL010923.

Chu, D., Y. Kaufman, C. Ichoku, L. Remer, D. Tanre, and B. Holben (2002), Validation of MODIS aerosol optical depth retrieval over land, *Geophys. Res. Lett.*, *29*(12), 8007, doi:10.1029/2001GL013205.

Chylek, P., and J. A. Coakley Jr. (1974), Aerosols and climate, *Sci*, *183*, 75–77, doi:10.1126/science.183.4120.75.

Chylek, P., U. Lohmann, M. Dubey, M. Mishchenko, R. Kahn, and A. Ohmura (2007), Limits on climate sensitivity derived from recent satellite and surface observations, *J. Geophys. Res.*, *112*, D24S04, doi:10.1029/2007JD008740.

Coakley, J. A., Jr., R. D. Cess, and F. B. Yurevich (1983), The effect of tropospheric aerosols on the Earths radiation budget: A parameterization for climate models, *J. Atmos. Sci.*, *40*(1), 116–138, doi:10.1175/1520-0469(1983)040<0116:TEOTAO>2.0.CO;2.

Diner, D. J., et al. (1998), Multi-angle Imaging SpectroRadiometer (MISR) description and experiment overview, *IEEE Trans. Geosci. Remote Sens.*, *36*(4), 1072–1087, doi:10.1109/36.700992.

Diner, D. J., R. Davies, T. Varnai, C. Moroney, C. Borel, S. A. W. Gerstl, and D. L. Nelson (1999), MISR level 2 top-of-atmosphere albedo algorithm theoretical basis, *Rep. D13401 Rev. D*, Jet. Propul. Lab., Pasadena, Calif., (Available at http://eospso.gsfc.nasa.gov/eos_homepage/for_scientists/atbd/docs/MISR/atbd-misr-08.pdf).

Diner, D. J., et al. (2001), MISR level 2 aerosol retrieval algorithm theoretical basis, *Rep. D11400 Rev. E*, Jet. Propul. Lab., Pasadena, Calif., (Available at http://eospso.gsfc.nasa.gov/eos_homepage/for_scientists/atbd/docs/MISR/atbd-misr-09.pdf).

Diner, D. J., et al. (2005), The value of multiangle measurements for retrieving structurally and radiatively consistent properties of clouds, aerosols, and surfaces, *Remote Sens. Environ.*, *97*, 495–518, doi:10.1016/j.rse.2005.06.006.

Hansen, J., M. Sato, A. Lacis, R. Ruedy, I. Tegen, and E. Matthews (1998), Climate forcings in the Industrial era, *Proc. Natl. Acad. Sci. U. S. A.*, *95*, 12,753–12,758, doi:10.1073/pnas.95.22.12753.

Hu, J., Y. Su, B. Tan, D. Huang, W. Yang, M. Schull, M. A. Bull, J. V. Martonchik, D. J. Diner, and Y. Knyazikhin (2007), Analysis of the MISR LAI/FPAR product for spatial and temporal coverage, accuracy and consistency, *Remote Sens. Environ.*, *107*, 334–347, doi:10.1016/j.rse.2006.06.020.

Intergovernmental Panel on Climate Change (2007), *IPCC Fourth Assessment Report: Climate change 2007*, Cambridge Univ. Press, Cambridge, U.K.

Isobe, T., E. D. Feigelson, M. G. Akritas, and G. J. Babu (1990), Linear regression in astronomy, *Astrophys. J.*, *364*, 104–113, doi:10.1086/169390.

Jin, Z., T. P. Charlock, W. L. Smith Jr., and K. Rutledge (2004), A parameterization of ocean surface albedo, *Geophys. Res. Lett.*, *31*, L22301, doi:10.1029/2004GL021180.

Kahn, R., P. Banerjee, and D. McDonald (2001), The sensitivity of multi-angle imaging to natural mixtures of aerosols over ocean, *J. Geophys. Res.*, *106*(D16), 18,219–18,238, doi:10.1029/2000JD900497.

Kahn, R., B. Gaitley, J. Martonchik, D. Diner, K. Crean, and B. Holben (2005), MISR global aerosol optical depth validation based on two years of coincident AERONET observations, *J. Geophys. Res.*, *110*, D10S04, doi:10.1029/2004JD004706.

Kalashnikova, O. V., and R. A. Kahn (2006), The ability of multi-angle remote sensing observations to identify and distinguish mineral dust types: 2. Sensitivity data analysis, *J. Geophys. Res.*, *111*, D11207, doi:10.1029/2005JD006756.

Kaufman, Y., D. Tanre, and O. Boucher (2002a), A satellite view of aerosols in the climate system, *Nature*, *419*, 215–223, doi:10.1038/nature01091.

Kaufman, Y. J., N. Gobron, B. Pinty, J.-L. Widlowski, and M. M. Verstraete (2002b), Relationship between surface reflectance in the visible and mid-IR used in MODIS aerosol algorithm theory, *Geophys. Res. Lett.*, *29*(23), 2116, doi:10.1029/2001GL014492.

Kinne, S., et al. (2006), An AeroCom initial assessment—Optical properties in aerosol component modules of global models, *Atmos. Chem. Phys.*, *6*, 1815–1834.

Liu, L., and M. I. Mishchenko (2008), Toward unified satellite climatology of aerosol properties: Direct comparisons of advanced level 2 aerosol products, *J. Quant. Spectrosc. Radiat. Transfer*, *109*, 2376–2385, doi:10.1016/j.jpsrt.2008.05.003.

Liu, Y., J. Sarnat, B. Coull, P. Koutrakis, and D. J. Jacob (2004), Validation of Multi-angle Spectroradiometer (MISR) aerosol optical thickness measurements using Aerosol robotic Network (AERONET) observations over the contiguous United States, *J. Geophys. Res.*, *109*, D06205, doi:10.1029/2003JD003981.

Loeb, N. G., and S. Kato (2002), Top-of-atmosphere direct radiative effect of aerosols over the tropical oceans from the Clouds and the Earths Radiant Energy System (CERES) satellite instrument, *J. Clim.*, *15*, 1474–1484, doi:10.1175/1520-0442(2002)015<1474:TOADRE>2.0.CO;2.

Loeb, N. G., and N. Manalo-Smith (2005), Top-of-atmosphere direct radiative effect of aerosols over global oceans from merged CERES and MODIS observations, *J. Clim.*, *18*, 3506–3526, doi:10.1175/JCLI3504.1.

Martonchik, J. V., D. J. Diner, R. Kahn, and B. Gaitley (2004), Comparison of MISR and AERONET aerosol optical depths over desert sites, *Geophys. Res. Lett.*, *31*, L16102, doi:10.1029/2004GL019807.

Mazzoni, D., M. Garay, R. Davies, and D. Nelson (2007), An operational MISR pixel classifier using Support Vector Machines, *Remote Sens. Environ.*, *107*, 149–158, doi:10.1016/j.rse.2006.06.021.

Mishchenko, M. I., I. V. Geogdzhayev, W. B. Rossow, B. Cairns, B. E. Carlson, A. A. Lacis, L. Liu, and L. D. Travis (2007), Long-term satellite record reveals likely recent aerosol trend, *Science*, *315*, 1543, doi:10.1126/science.1136709.

Miura, T, H. Yoshioka, K. Fujiwara, and H. Yamamoto (2008), Intercomparison of ASTER and MODIS surface reflectance and vegetation index products for synergistic applications to natural resource monitoring, *Sensors*, *8*, 2480–2499, doi:10.3390/s8042480.

Patadia, F., P. Gupta, and S. A. Christopher (2008), First observational estimates of global clear sky shortwave aerosol direct radiative effect over land, *Geophys. Res. Lett.*, *35*, L04810, doi:10.1029/2007GL032314.

Quinn, P. K., and T. S. Bates (2005), Regional aerosol properties: Comparisons of boundary layer measurements from ACE 1, ACE 2, Aerosols99, INDOEX, ACE Asia, TARFOX, and NEAQS, *J. Geophys. Res.*, *110*, D14202, doi:10.1029/2004JD004755.

Quinn, P. K., T. S. Bates, D. J. Coffman, T. L. Miller, J. E. Johnson, D. S. Covert, J. P. Putaud, C. Neususs, and T. Novakov (2000), A comparison of aerosol chemical and optical properties from the 1st and 2nd Aerosol Characterization Experiments, *Tellus, Ser. B*, *52*, 239–257, doi:10.1034/j.1600-0889.2000.00033.x.

Remer, L. A., and Y. J. Kaufman (2006), Aerosol direct radiative effect at the top of the atmosphere over cloud free ocean derived from five years of MODIS data, *Atmos. Chem. Phys.*, *6*, 237–253.

Ricchiazzi, P., C. Gautier, J. A. Ogren, and B. Schmid (2006), A comparison of aerosol optical properties obtained from in situ measurements and retrieved from Sun and sky radiance observations during the May 2003 ARM Aerosol Intensive Observation Period, *J. Geophys. Res.*, *111*, D05S06, doi:10.1029/2005JD005863.

Satheesh, S. K. (2002), Aerosol radiative forcing over land: Effect of surface and cloud reflection, *Ann. Geophys.*, *20*, 2105–2109.

Scepan, J., G. Menz, and M. C. Hansen (1999), The DISCover validation image interpretation process, *Photogramm. Eng. Remote Sens.*, *1999*(9), 1075–1081.

Schuster, G. L., O. Dubovik, and B. N. Holben (2006), Angstrom exponent and bimodal aerosol size distributions, *J. Geophys. Res.*, *111*, D07207, doi:10.1029/2005JD006328.

Sun, W., N. G. Loeb, R. Davies, K. Loukachine, and W. F. Miller (2006), Comparison of MISR and CERES top-of-atmosphere albedo, *Geophys. Res. Lett.*, *33*, L23810, doi:10.1029/2006GL027958.

Tucker, C. J., and P. J. Sellers (1986), Satellite remote sensing of primary productivity, *Int. J. Remote Sens.*, *7*, 1395–1416, doi:10.1080/01431168608948944.

Yu, H., R. E. Dickinson, M. Chin, Y. J. Kaufman, M. Zhou, Y. Tian, O. Dubovik, and B. N. Holben (2004), The direct radiative effect of aerosols as determined from a combination of MODIS retrievals and GOCART simulations, *J. Geophys. Res.*, *109*, D03206, doi:10.1029/2003JD003914.

Yu, H., et al. (2006), A review of measurement-based assessments of the aerosol direct radiative effect and forcing, *Atmos. Chem. Phys.*, *6*, 613–666.

Y. Chen and J. T. Randerson, Department of Earth System Science, University of California, Irvine, 3317 Croul Hall, Irvine, CA 92697, USA. (yang.chen@uci.edu; jranders@uci.edu)

D. J. Diner, Jet Propulsion Laboratory, California Institute of Technology, MS 169-237, 4800 Oak Grove Drive, Pasadena, CA 91109, USA. (david.j.diner@jpl.nasa.gov)

R. A. Kahn, NASA Goddard Space Flight Center, Code 613.2, Greenbelt, MD 20771, USA. (ralph.kahn@nasa.gov)

Q. Li, Department of Atmospheric and Oceanic Sciences, University of California, Los Angeles, 7220 Mathematical Sciences Building, Los Angeles, CA 90095, USA. (qli@atmos.ucla.edu)